JOURNAL OF MATERIALS SCIENCE 29 (1994) 2192–2204

Trapped cracks at indentations

Part II *Fracture mechanics model*

R. F. COOK
IBM Research Division, T. J. Watson Research Center, Yorktown Heights, New York, 10598, USA
L. M. BRAUN
Ceramics Division, National Institute of Standards and Technology, Gaithersburg, MD 20899, USA

A fracture-mechanics model for indentation cracking in phase-transforming materials is developed, based on the competing interaction of the tensile residual-mismatch field and the compressive contact-induced transformation field. In addition to the usual subthreshold and well-developed cracking ranges, the model predicts the trapping of cracks at indentations, within the transformation zone. As an example, the model is used to describe the dependence of radial crack length on indentation load in a range of yttria–tetragonal zirconia polycrystals (Y–TZP), explicitly addressing the trapping behaviour observed in Part I. The crucial parameters of the model obtained from the experimental fits, the size of the transformation zone relative to the contact impression, *b*/*a*, and the magnitude of the transformation stress relative to the hardness, σ_T/H, agree with independent measurements. Although applied to phase-transforming materials here, the principles of the model are generally applicable to systems with short-range, compensating stress fields competing with longer-ranged, dominant fields, leading to two discrete crack populations.

Nomenclature

a	Contact-impression semi-diagonal
b	Contact-induced transformation-zone dimension
c	Total crack length, $c = l + s$
c_n	Contact impression crack nucleus dimension, $c_n < s$
f	Stress-intensity factor weighting term, $K = (Ha^{1/2})f$
H	Hardness
K_r	Residual stress-intensity factor
K_t	Transformation stress-intensity factor
l	Radial crack length
P	Indentation load
s	Contact-impression tensile-zone dimension
T_1	Toughness in the transformation zone
T_2	Toughness outside the transformation zone
α	Stress coefficient, $\sigma = \alpha H$
σ_r	Residual-stress-field amplitude
σ_t	Transformation-stress-field amplitude
ψ_1	Crack-geometry parameter in the transformation zone
ψ_2	Crack-geometry parameter outside the transformation zone

1. Introduction

In Part I of this series, the effects of a contact-induced transformation zone on indentation cracks in yttria-doped tetragonal zirconia polycrystals (Y–TZP) were examined [1]. A particular effect was that radial cracks could be "trapped" within the zone by the compressive stress associated with the tetragonal-to-monoclinic phase transformation. Here in Part II, a fracture-mechanics model is developed for trapped cracks at indentations, and this model is used to describe the experimental data from Part I.

The key experimental observations to be included in the model are summarized in Fig. 1. Below a threshold indentation load, no radial cracks are initiated. Above this threshold, trapped cracks are initiated, although not at every impression corner and varying considerably in length. Above a larger, escape indentation load, well-developed cracks are formed, although again not at every impression corner, but with little variation in length. At a very large indentation load, only well-developed cracks are formed. The two thresholds (initiation and escape), the decrease in the variability of the crack lengths (from trapped to well-developed), the overlapping cracking behaviour (trapped with subthreshold, and well-developed with trapped), the general increase in crack length with indentation load, and the linear indentation-load–crack length behaviour of the well-developed cracks will all be included.

The model is based on the integration of two stress fields, which are assumed to maintain a geometrical similarity with the indentation, to obtain two superposed stress-intensity factors. The first stress-intensity factor is derived from the distributed, tensile, residual-mismatch stress and contains a maximum. A component of this factor is similar to that in previous models

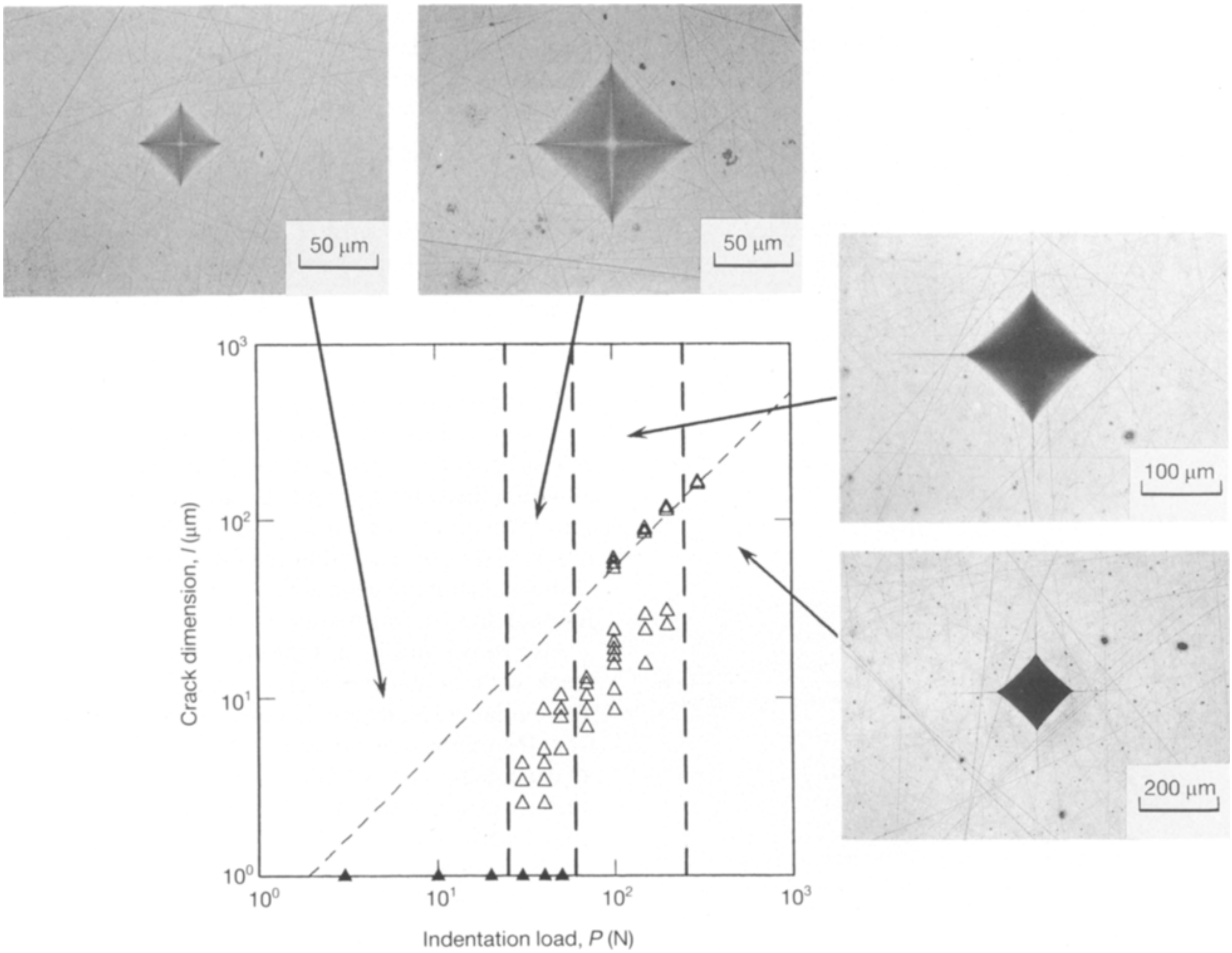

Figure 1 A plot of radial crack length, l, versus indentation load, P, for a Y-TZP material (0.42 μm grain size). (▲) Subthreshold loads, (△) individual crack-length measurements. (¦) Divides the indentation-load range into four regions of behaviour: subthreshold, trapped, mixed trapped and well-developed, and well-developed only (in order of increasing P). The micrographs show examples from each region.

considering crack initiation at expanding inclusions [2–6] and in materials with thermal-expansion anisotropy [7], in which the crack propagates in a monotonically decreasing stress field. Another component is similar to that in previous models of crack initiation at indentations [8–14], which often contain an increasing stress at small crack lengths. The second stress-intensity factor is derived from the localized, compressive, transformation stress, and contains a minimum. The superposition of the two stress-intensity factors leads to a "double-humped" net stress-intensity factor, similar to that describing ring and cone cracks at Hertzian contacts [15–17].

We begin with a description of the indentation stress fields and the derivation of the residual and transformation stress-intensity factors. This is followed by a general description of the resulting initiation and trapping mechanics for the simple case of cracks with invariant geometry propagating in materials with invariant toughness. Modifications to these mechanics are then made for a more realistic approximation for transformation-toughening materials, in which the crack geometry and material toughness change as the crack extends across the transformation-zone boundary. The next sections describe the procedure used to fit the model to the data, followed by the resulting fits and parameter evaluations. The discussion centres on the use of the model for description of other trapped-crack systems and in materials optimization.

2. Stress fields and stress-intensity factors

2.1. Indentation stress field

Fig. 2 is a schematic diagram of the residual contact impression of an indentation, the associated contact-induced transformation zone, and their respective stress fields. The semi-diagonal of the contact impression, a, is a measure of the scale of the plastic-deformation zone, and is related to the peak contact load, P, and the hardness, H (the projected contact stress), by

$$a = (P/2H)^{1/2} \qquad (1)$$

The contact-induced transformation zone extends a characteristic distance, b, beyond the impression corner. This extent is determined by a compromise between the chemical-energy decrease associated with the tetragonal-to-monoclinic phase transformation and surface- and strain-energy increases associated with the expanding monoclinic particles in the surrounding tetragonal matrix [18]. Although the local radius of the transformation zone shows some variability, reflecting local variations in the metastability of

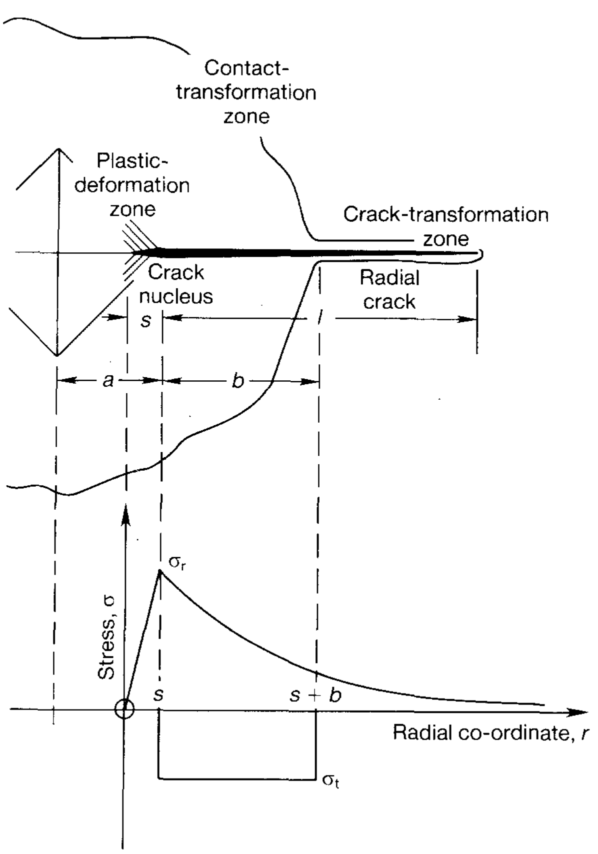

Figure 2 A schematic diagram of the indentation system showing the dimensions of the plastic-deformation and phase-transformation zones, the behaviour of their associated stress fields, and the radial-crack dimensions.

the monoclinic phase (see Fig. 2 in Part [1]), the average radius is well-defined for a given material and maintains geometrical similarity with the contact impression [19] such that the ratio b/a is invariant with indentation load.

The stress field arising from the strain mismatch of the plastic-deformation zone embedded in the surrounding matrix is composed of two components. Inside the zone the circumferential stress acting on a prospective radial-crack plane is predominantly compressive. However, close to the zone boundary the stress becomes tensile [8, 10, 12, 14], and reaches a maximum value at the boundary. Similar to previous works [8, 10, 14] this component is modelled as a linear increase

$$\sigma_r(r) = \sigma_R(r/s), \quad 0 \leqslant r \leqslant s \tag{2a}$$

where s is the length scale within the deformation zone over which the tensile stress acts, σ_R is the maximum stress at the zone boundary, and the origin of the co-ordinate system, $r = 0$, is fixed at the edge of the tensile region, see Fig. 2 (rather than at the deformation-zone boundary [8, 9, 13]). The choice of origin reflects the supposition that radial cracks are initiated from shear-fault nuclei located within the deformation zone [9, 14, 20–24] beginning at this origin. (The nuclei and the ensuing radial cracks may also be stabilized and propagated by shear stresses within the zone [9, 11, 13, 14, 22, 23], but these effects are neglected here.) The tensile region within the zone is also assumed to maintain geometrical similarity, such that the ratio s/a is constant. Outside the plastic-deformation zone, the stress field is modelled as that belonging to an expanding spherical cavity, and decreases with distance from the zone edge according to [4, 12, 14]

$$\sigma_r(r) = \sigma_R(s/r)^3, \quad r > s \tag{2b}$$

The stress σ_R will be related to the hardness.

The stress field arising from the transformation zone is modelled as a simple circular step function

$$\begin{aligned} \sigma_t(r) &= \sigma_T \quad s < r \leqslant s + b \\ &= 0 \quad 0 \leqslant r \leqslant s \text{ and } r > s + b \end{aligned} \tag{3}$$

Observations of surface uplift and measurements of the fraction of transformed monoclinic phase [1, 19, 25] suggest that this is not a bad approximation, although there are undoubtedly drop-off effects at the transformation-zone boundary and some transformation stresses exerted within the deformation zone. As s and b maintain geometrical similarity, so do the residual and transformation stress fields.

Also shown in Fig. 2 is the surface trace of a radial crack with its associated crack transformation zone. The radial-crack length is conventionally measured from the impression corner as l. However, in this case, an extended crack system is used, measured from the nucleus origin inside the deformation zone, with a total length of $c = l + s$. Fig. 3 is an optical micrograph of the radial system, showing the crack origin a distance s inside the deformation zone. Radial cracks will only be regarded as being initiated for $l > 0$, i.e. for $c > s$, although calculations of the stress-intensity factors driving the crack are made for all $c > 0$. (Some works have set $c = l + a$, and performed stress-intensity-factor calculations for $c > a - s$ [11, 12, 14].) The Nomenclature provides a definition of all the parameters used here.

Fractographic observations and sectioning experiments suggest that the surface traces are those of shallow cracks extending predominantly along the surface, remaining disconnected under the contact im-

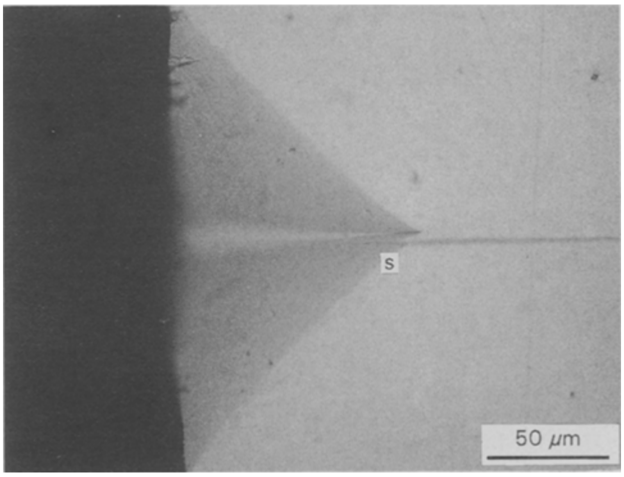

Figure 3 An optical micrograph (in reflected light) of a broken indentation in a Y–TZP material (0.42 μm grain size). The unbroken radial crack clearly nucleates within the plastic deformation zone near the contact impression corner and extends a distance S relative to the impression dimension before initiating. Measurements of S provide an estimation of the size of the tensile region within the deformation zone.

pression in the bulk of the material (see the references in [1] and [26, 27]). An additional observation, crucial to the modelling here, is that cracking behaviour across the contact impression is frequently dissimilar; that is, one crack is trapped while the other is well-developed, or one crack is subthreshold and the other is trapped. Such observations suggest that the two opposing surface traces are not those of a single crack (although their behaviour might be coupled under subsequent loadings [28]). Hence, the surface traces are taken to be representative of essentially linear cracks, extending to a depth approximately equal to that of the deformation zone.

The crack-transformation zone for the well-developed radial crack in Fig. 2 is shown with constant width, implying that the transformation toughening for such a crack has saturated to the steady-state level [18]. Toughness, or fracture-resistance aspects of this problem will be considered in detail later. The following sections use the stress states described here to develop the driving forces for fracture, the residual and transformation stress-intensity factors, K_r and K_t, respectively.

2.2. Residual stress-intensity factor

The general equation used for calculating the stress-intensity factors from the stress distributions was

$$K(c) = \frac{2\psi c^{1/2}}{\pi} \int_0^c \frac{\sigma(r)\,dr}{(c^2 - r^2)^{1/2}} \qquad (4)$$

where the kernel function for a linear crack has been used [29], but a geometrical prefactor of $\psi/\pi^{1/2}$ has been included. The difference of this factor from unity accounts for the true geometry of the radial cracks and free-surface effects.

Conventional indentation-fracture mechanics uses the stress field outside the plastic-deformation zone, given by Equation 2b, in Equation 4 to generate a residual stress-intensity factor, given in this case by K_r^{outer}. Taking advantage of the assumed geometrical similarity of the problem, normalized variables are set as

$$\begin{aligned} \rho &= r/a \\ C &= c/a \qquad (5) \\ S &= s/a \end{aligned}$$

such that K_r^{outer} is given by a dimensionless integral

$$K_r^{\text{outer}} = \frac{2\psi}{\pi} \sigma_R a^{1/2} C^{1/2} S^3 \int_S^C \frac{d\rho}{\rho^3 (C^2 - \rho^2)^{1/2}} \qquad (C > S) \qquad (6)$$

The residual-stress amplitude is conveniently reduced to a dimensionless variable, α_R, via the hardness:

$$\sigma_R = \alpha_R H \qquad (7)$$

Completing the integral in Equation 6 thence gives the requisite stress-intensity factor as

$$K_r^{\text{outer}} = (Ha^{1/2}) f_r^{\text{outer}}(C, \alpha_R, S) \qquad (8a)$$

which is the product of a term controlling the scale of the event, $(Ha^{1/2})$, and a scale-invariant, crack-length dependent, weighting term

$$f_r^{\text{outer}} = \frac{2\psi\alpha_R}{\pi} C^{1/2} S^3 \left[\frac{(C^2 - S^2)^{1/2}}{2C^2 S^2} + \frac{1}{2C^3} \ln\left(\frac{C + (C^2 - S^2)^{1/2}}{S} \right) \right] \qquad C > S; \quad (8b)$$

this equation includes the material and geometrical parameters ψ, α_R and S. The large-crack asymptotic limit of this weighting term is

$$f_r^{\text{outer}} \rightarrow \frac{\psi \alpha_R S}{\pi C^{1/2}} \quad \text{as } C \rightarrow \infty \qquad (9)$$

which contains the familiar $C^{-1/2}$-dependence for a line-loaded crack [29].

The second component of the residual stress-intensity factor, K_r^{inner}, is obtained by inserting Equation 2a in Equation 4 to gain

$$K_r^{\text{inner}} = \frac{2\psi}{\pi} \sigma_R a^{1/2} \frac{C^{1/2}}{S} \int_0^C \frac{\rho\, d\rho}{(C^2 - \rho^2)^{1/2}} \qquad (C \geqslant 0) \qquad (10)$$

using the normalized variables as before. On integration this gives

$$K_r^{\text{inner}} = (Ha^{1/2}) f_r^{\text{inner}}(C, \alpha_R, S) \qquad (11a)$$

where the weighting term is

$$\begin{aligned} f_r^{\text{inner}} &= \frac{2\psi\alpha_R}{\pi} \frac{C^{3/2}}{S} \qquad (0 \leqslant C < S) \\ &= \frac{2\psi\alpha_R}{\pi} \frac{C^{3/2}}{S} \left[1 - (1 - S^2/C^2)^{1/2}\right] \qquad (C > S) \qquad (11b) \end{aligned}$$

The large-crack asymptotic limit of this weighting term is identical to that for f_r^{outer}:

$$f_r^{\text{inner}} \rightarrow \frac{\psi \alpha_R S}{\pi C^{1/2}} \quad \text{as } C \rightarrow \infty \qquad (12)$$

The small-crack behaviour, Equation 11b, is more destabilizing than that of the familiar uniform stress ($C^{3/2}$ compared with $C^{1/2}$ [29]) – a reflection of the increasing stress in this region.

The total residual stress-intensity factor is given by the sum of the inner and outer terms,

$$K_r = (Ha^{1/2}) f_r(C, \alpha_R, S) \qquad (13a)$$

where the overall weighting term is given by

$$f_r = f_r^{\text{inner}} + f_r^{\text{outer}} \qquad (13b)$$

Fig. 4 plots the residual weighting term, showing the individual components and the asymptotic limits, using $\alpha_R = 0.1$, $S = 0.3$ and $\psi = 3.5$.

2.3. Transformation stress-intensity factor

The transformation stress-intensity factor, K_t, is obtained by using Equation 3 in Equation 4 to give

$$K_t = \frac{2\psi}{\pi} \sigma_T a^{1/2} C^{1/2} \int_0^C \frac{d\rho}{(C^2 - \rho^2)^{1/2}} \qquad (14)$$

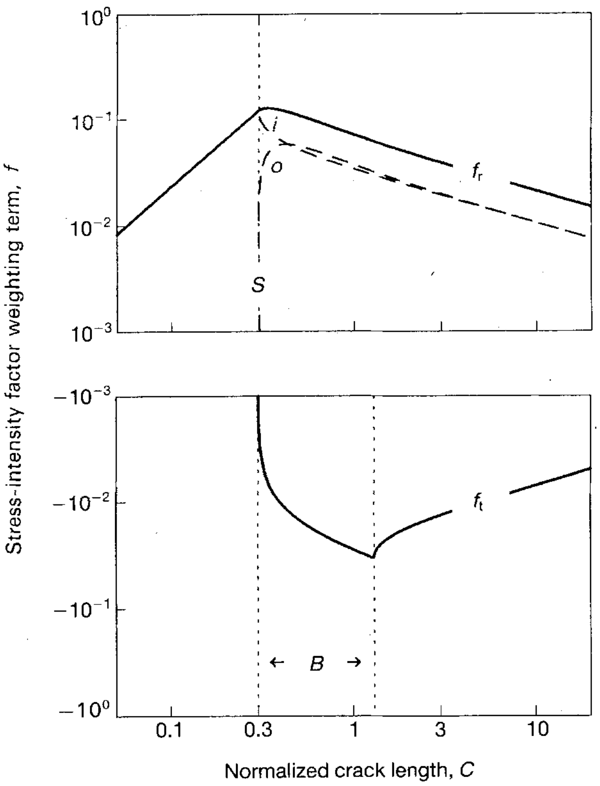

Figure 4 Plot of the dimensionless stress-intensity factor weighting terms versus the normalized crack length, C. The residual term, f_r is positive with $C^{3/2}$ and $C^{-1/2}$ asymptotic dependencies at small and large crack lengths, respectively. (The components of the residual term, f_r^{inner} and f_r^{outer}, deriving from residual-stress components inside and outside the plastic-deformation zone are shown by the dashed lines.) The transformation term, f_t, is negative and has $-C^{-1/2}$ asymptotic dependence at large crack lengths.

using Equation 5. Normalizing the transformation-zone dimension and the transformation stress as

$$B = b/a \qquad (15)$$

and

$$\sigma_T = \alpha_T H \qquad (16)$$

gives the integrated stress-intensity factor as

$$K_t = (Ha^{1/2}) f_t(C, \alpha_T, S, B) \qquad (17a)$$

with a weighting term of

$$\begin{aligned} f_t &= 0 \quad (0 \leqslant C \leqslant S) \\ &= \frac{2\psi\alpha_T}{\pi} C^{1/2}\left[\pi/2 - \sin^{-1}\left(\frac{S}{C}\right)\right] \\ &\qquad \times (S < C \leqslant S + B) \\ &= \frac{2\psi\alpha_T}{\pi} C^{1/2}\left[\sin^{-1}\left(\frac{S+B}{C}\right) \right. \\ &\qquad \left. - \sin^{-1}\left(\frac{S}{C}\right)\right] \quad (C > S + B) \qquad (17b) \end{aligned}$$

The large-crack asymptotic limit of this weighting term is

$$f_t \rightarrow \frac{2\psi\alpha_T B}{\pi C^{1/2}} \quad \text{as } C \rightarrow \infty \qquad (18)$$

It should be noted that the transformation stress is compressive, and hence α_T, and thus f_t and K_t, are all negative. Fig. 4 is a plot of this weighting term showing the asymptotic limit, and using $\alpha_T = -0.01$ and $B = 1.0$.

The total stress-intensity factor is the sum of the residual and transformation terms

$$K(c) = K_r(c) + K_t(c) \qquad (19a)$$

such that the normalized form is

$$\begin{aligned} K(C) &= K_r(C) + K_t(C) \\ &= (Ha^{1/2}) f(C, \alpha_R, \alpha_T, S, B) \qquad (19b) \end{aligned}$$

where the full weighting term is a similar sum

$$f(C) = f_r(C, \alpha_R, S) + f_t(C, \alpha_T, S, B) \qquad (19c)$$

Noting that S and B are invariant with P, the dimensionless weighting term, f, is also seen to be a geometrically-similar function.

3. General initiation mechanics

The stress-intensity factor of Equation 19 allows for a full description of the cracking behaviour as a function of the indentation load. This section considers initiation, trapping, escape and well developed cracking phenomena for materials in which the crack geometry, characterized by ψ, and the toughness, T, are invariant with the crack length, c, providing the background mechanics for the following section where these constraints are lifted.

3.1. Initiation

Consider a radial-crack nucleus extending from the origin within the plastic-deformation zone to a characteristic length $c_n \leqslant s$ (Fig. 2). The nucleus is stabilized by shear processes within the zone such that it maintains geometrical similarity with the contact impression

$$C_n = c_n/a \qquad (20)$$

where the normalized nucleus dimension, C_n, is a constant. Although the overall geometrical similarity enforces a fixed tensile stress profile over the nucleus (Equation 2a), the stress-intensity factor on the nucleus, increases with increasing impression size, and therefore with indentation load (Equation 11).

For $K(C_n) < T$, the nucleus remains metastably trapped in the zone. For $K(C_n) = T$, the nucleus is in a position of unstable equilibrium ($\mathrm{d}K/\mathrm{d}c > \mathrm{d}T/\mathrm{d}c$), and it initiates into a crack. The equilibrium condition is (from Equation 19)

$$(Ha_{*1}^{1/2}) f_{*1} = T \qquad (21)$$

such that the critical impression size and indentation load (from Equation 1) are given by

$$\begin{aligned} a_{*1} &= (T/H)^2 f_{*1}^{-2} \\ P_{*1} &= 2(T^4/H^3) f_{*1}^{-4} \qquad (22) \end{aligned}$$

yielding the familiar dependencies for geometrically similar problems [8–14] of a_{*1} and P_{*1} on the material parameters T and H, and on the geometrical weighting term

$$f_{*1} = f(C_n) = f_r^{\text{inner}}(C_n) \qquad (23)$$

from Equations 13 and 19.

Fig. 5 is a plot of the normalized stress-intensity factor K/T as a function of the normalized crack length, C, at the initiation condition $a = a_{*1}$, using the variables used in Fig. 4 and using $C_n = 0.25$. The double-humped nature of the stress-intensity factor with two destabilizing-to-stabilizing sequences is apparent. The initiation condition is fulfilled as the first destabilizing branch intersects the toughness line ($K/T = 1$) at the nucleus crack length ($C = C_n$). The double-logarithmic plotting scheme used in Fig. 5 shows the asymptotic responses of the first destabilizing and second stabilizing branches as straight lines with gradients of 3/2 and − 1/2, respectively, following Equation 9, 11, 12 and 18. Fig. 6 is a plot of the stress-intensity factor for a range of a-values (an advantage of the plotting scheme is that changes in a appear as simple vertical translations of the curve in Fig. 5). The curve labelled a_{*1} corresponds to the initiation conditions, with the equilibrium instability point indicated by the open circle. The curve labelled a_0 corresponds to the metastably trapped, subthreshold condition.

3.2. Trapping

For indentation loads $P \geqslant P_{*1}$, the initiated cracks may be trapped in the transformation zone under conditions of stable equilibrium ($\mathrm{d}K/\mathrm{d}c < \mathrm{d}T/\mathrm{d}c$).

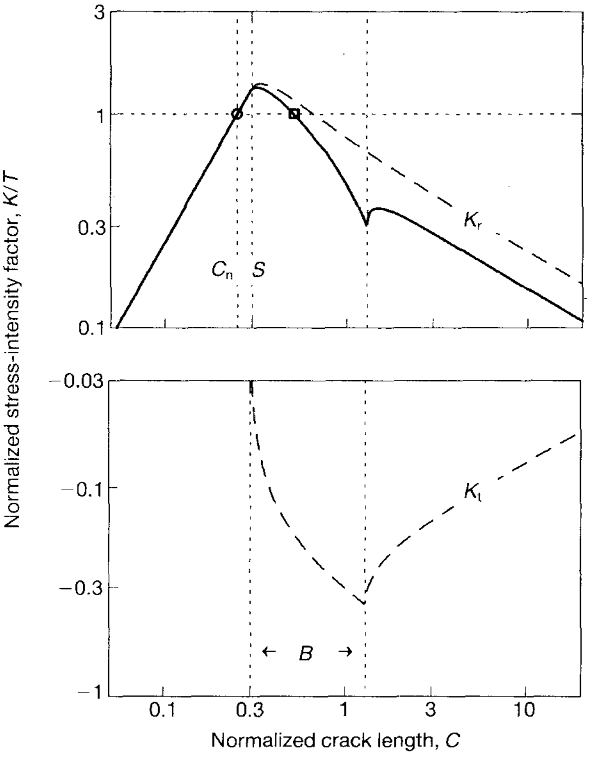

Figure 5 A plot of normalized stress-intensity factor K/T versus normalized crack length, C, for a trapped radial-crack system at initiation ($K = T$ and $\mathrm{d}K/\mathrm{d}C > \mathrm{d}T/\mathrm{d}C$ at $C = C_n$). (——) The total stress-intensity factor, and (– – –) the initiating (residual) and trapping (transformation) components.

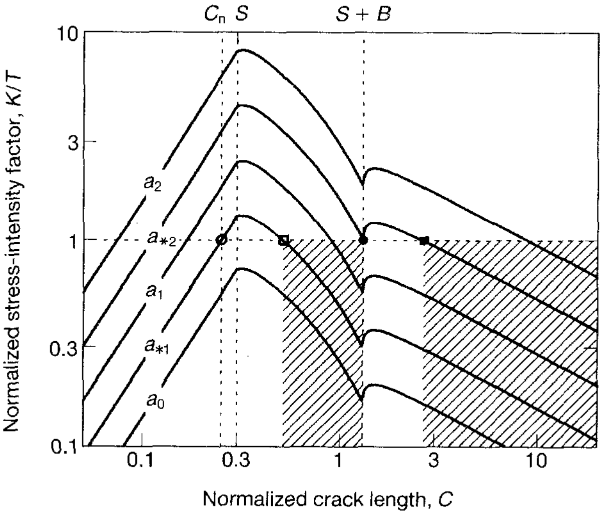

Figure 6 A plot of normalized stress-intensity factor, K/T, versus normalized crack length, C, for a trapped radial-crack system at a range of indentation-impression sizes: a_0 (subthreshold) < a_{*1} (initiation) < a_1 (trapped) < a_{*2} (escape) < a_2 (well-developed). (○, □) unstable and stable *trapped* configurations and (●, ■) unstable and stable *well-developed* configurations. The hatched regions represent the ranges of trapped (small) and well-developed (large) cracks.

There is a minimum trapped crack length

$$C_t = c_t/a_{*1} = (l_t + s)/a_{*1}$$
$$= L_t + S \qquad (24)$$

such that $K(C_t) = T$ and thus

$$(Ha_{*1}^{1/2})f_{\min} = T \qquad (25)$$

where

$$f_{\min} = f(C_t) \qquad (26)$$

This stable equilibrium point is indicated by the open square in Fig. 5 and on the curve labelled a_{*1} in Fig. 6. Greater trapped crack lengths may be generated, as shown by the curve labelled a_1.

3.3. Escape

At $C = S + B$, the stress-intensity factor abruptly changes from stabilizing to destabilizing. Hence the criterion $K(S + B) = T$ defines an unstable equilibrium at which cracks can escape from the transformation zone. Imposing the equilibrium condition at this point yields

$$(Ha_{*2}^{1/2})f_{*2} = T \qquad (27)$$

where the critical impression size and indentation load are now

$$a_{*2} = (T/H)^2 f_{*2}^{-2}$$
$$P_{*2} = 2(T^4/H^3)f_{*2}^{-4} \qquad (28)$$

with material and geometrical dependencies as before (Equation 22) for a_{*2} and P_{*2}, and the weighting term is

$$f_{*2} = f(S + B) \qquad (29)$$

The indentation load P_{*2} is the upper bound for the existence of trapped cracks, and hence $P_{*1} \leqslant P < P_{*2}$ is the trapping-load range with $a_{*1} \leqslant a < a_{*2}$ the conjugate impression-size range. The corresponding range of trapped crack lengths is $C_t \leqslant C < (S + B)$; this is indicated by the left hatched band in Fig. 6. The unstable equilibrium point for escape is marked by the closed circle on the curve labelled a_{*2}.

3.4. Well-developed cracks

For $P \geqslant P_{*2}$, the escaped cracks are well-developed in stable equilibrium outside the transformation zone. There is a minimum well-developed crack length given by $C_w > (S + B)$ such that $K(C_w) = (Ha_{*2}^{1/2}) f(C_w) = T$; this is indicated by the solid square on the curve labelled a_{*2} in Fig. 6. Greater well-developed crack lengths may be generated, as shown by the curve labelled a_2, and the range of well-developed cracks, $C \geqslant C_w$, is indicated by the right hatched band.

For $P \gg P_{*2}$ the indentation crack length is given by

$$(Ha^{1/2}) f_{\max} = T \tag{30}$$

where $f_{\max}$ is evaluated in the limit $C \to \infty$, such that

$$f_{\max} = \frac{2\psi}{\pi}\left(\frac{\alpha_R S}{2C^{1/2}} + \frac{\alpha_R S}{2C^{1/2}} + \frac{\alpha_T B}{C^{1/2}}\right) \tag{31}$$

from Equations 9, 12 and 18. In this limit $C = L + S \approx L$, so that denormalizing the crack length yields the experimentally observed linear relationship between the indentation load and the radial crack length for well-developed cracks:

$$P/l = \frac{2(T^2/H)}{(2\psi/\pi)^2(\alpha_R S + \alpha_T B)^2} \tag{32}$$

using Equation 1. In the usual description of Palmqvist, or radial, cracks [1, 17, 30, 31], the mechanical energy release rate $\mathscr{G} = \beta P/l$. Using $\mathscr{G} = K^2/E$ in Equation 32 provides $\beta = 2(H/E)(\psi/\pi)^2(\alpha_R S + 2\alpha_T B)^2$.)

4. Initiation mechanics for transforming materials

In order to fit the experimental observations, the initiation mechanics described in the previous section were modified in two ways. The first modification took into account the transformation toughening in these materials. In the transformation zone a large number of tetragonal-phase grains were transformed to monoclinic-phase in order to accommodate the indentation contact strain. These grains were therefore not available for stress-induced transformation to give rise to toughening as a crack advanced through the zone. Outside the zone, many more grains were available for transformation toughening, and hence there was an increase in the toughness of the material across the transformation-zone boundary. This was modelled here as a simple step-function increase

$$\begin{aligned} T &= T_1 \quad (C \leqslant (S + B)) \\ &= T_2 \quad (C > (S + B) \end{aligned} \tag{33}$$

T-curve (or R-curve) effects (arising from a transient in the crack-tip transformation zone) were ignored. Measurements in Y–TZP materials suggest that the T-curves are extremely steep [32] and saturate at crack lengths considerably less than the distance the well-developed cracks extend beyond the zone boundary. However, as alluded to earlier, close observation [1] suggests that there is not a sharp boundary for the zone of strain-induced transformation. Hence, the increase in toughness from T_1 to T_2 was probably more gradual than the step function used.

The second modification took into account the change in geometry from trapped to well-developed cracks [28]. In the trapped state, the indentation cracks were considerably more shallow than those in the well-developed state. To account for the decreased mechanical-energy release rate for trapped and initiated cracks, relative to the well-developed cracks, a reduced geometry factor was used in this region

$$\begin{aligned} \psi &= \psi_1 \quad (C \leqslant (S + B)) \\ &= \psi_2 = 2\psi_1 \quad (C > (S + B)) \end{aligned} \tag{34}$$

with an arbitrary factor-of-two increase across the transformation-zone boundary. Once again, the actual change in crack morphology was probably more gradual at $C \to S + B$ than the step function used here.

Fig. 7 is a plot of the normalized stress-intensity factor, K/T_1, as a function of normalized crack length, C. The a-values and symbols are as in Fig. 6. Comparison with Fig. 6 shows that the effect of the geometry modification is to deepen the trapping-well between the initiation and well-developed branches of the curve, particularly in comparison to the toughness increase at the zone boundary. However, there is a trade-off between T and ψ in determining the loads for both initiation (Equations 11 and 22) and escape (Equations 17 and 28), and the lengths of both trapped (Equations 13 and 25) and well-developed (Equations

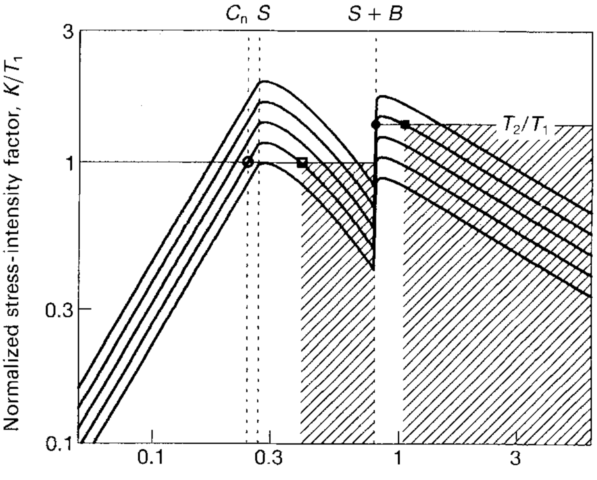

Figure 7 A plot of normalized stress-intensity factor, K/T_1, versus normalized crack length, C, for a trapped radial-crack system in a transforming material in which the crack geometry and material toughness increase across the transformation-zone boundary. The notation is the same as in Fig. 6. Parameters are taken from Tables I and II for the 0.36 μm grain-size material.

17 and 32) cracks. Hence, the combined effect of the modifications is to decouple the initiation and escape events and their associated minimum crack lengths, without necessarily altering the ratios P_{*1}/P_{*2} or C_t/C_w. (For $T_2 = 2T_1$, the ratios are unaltered.)

5. Experimental fitting procedure

In order to fit the model to experimental data on Y–TZP, the parameters α_T, B, T_1, and C_n, were determined by fitting to the experimental variables P/l, P_{*2}, P_{*1} and l_t, as described below. Other parameters were determined by experimental observation.

The parameter $S = s/a$ was determined from observations of approximately ten 300 N indentations in each material. s was taken to be the largest observed extent of a radial crack within the plastic deformation zone (see Figs 2 and 3). The hardness, H, was taken from measurements for each material [1]. Similarly, the toughness outside the transformation zone, T_2, was set as the measured steady-state T_∞-value for each material [1]. Table I gives the S, H and T_2-values. The parameter α_R was set for all materials at 0.1, consistent with recent evaluations on a range of glasses [14] (previous estimations for a variety of materials are in the range 0.1 to 0.22 [8–13]).

The α_T and B-parameters were determined by fitting to the well-developed crack response, P/l, and the escape load P_{*2}. Inverting Equations 28 and 32 gives

$$f_{*2} = f_{*2}(S, B) = \left[\frac{2(T_2^4/H^3)}{P_{*2}}\right]^{1/4}$$

$$(2\psi_2/\pi)(\alpha_R S + \alpha_T B) = \left[\frac{2(T_2^2/H)}{(P/l)}\right]^{1/2} \qquad (35)$$

Simultaneous solution of these equations yielded α_T and B.

The T_1-parameter was determined from the minimum trapped crack length, l_t, and the initiation load, P_{*1}. Combining Equations 1 and 25 and inverting gives the following equation

$$T_1 = f_{\min}(2/H^3 P_{*1})^{1/4} \qquad (36)$$

and T_1, using α_T from above.

The C_n-parameter was determined from the initiation load, P_{*1}. Combining Equations 11, 22 and 23 gives

$$C_n = (\pi S/2\psi_1 \alpha_R)^{2/3} (2T_1^4/H^3 P_{*1})^{1/6} \qquad (37)$$

using T_1 from above.

The values of the experimental variables were chosen so as to yield upper and lower bounds of the predicted radial crack length at a given indentation load. The upper-bound (lower-bound) value for P/l was taken as the least (greatest) value that allowed the model to predict an escaped crack length. The upper-bound (lower-bound) value for P_{*2} was taken as the smallest (largest) indentation load at which a trapped crack was observed. The upper-bound (lower-bound) value for l_t was taken as the longest (shortest) observed trapped crack length at $P = P_{*1}$. A common value of P_{*1} for both bounds was taken as the smallest indentation load at which a (trapped) crack was observed. Fig. 8 illustrates the ranges of the bounding parameters. The mean response for a material was determined using the geometric means of the bounding-values. Table I gives the geometric means of the experimental indentation parameters P/l, P_{*2}, P_{*1}, and l_t.

Consideration of the above shows that there remains only one arbitrary adjustable parameter – the geometry parameter ψ_2 (and thus ψ_1). In determining the model parameters from the experimental data, the greatest value of ψ_2 was chosen subject to two constraints: the transformation stress cannot be tensile, i.e. $\alpha_T < 0$, and the toughness in the transformation zone cannot be less than that of untoughened ZrO_2, i.e. $T_1 > 2$ MPa m$^{1/2}$ [18].

Once the parameters were determined, the $l(P)$ response was calculated by numerically searching for the stable crack length at a given indentation load. For $P < P_{*1}$, no cracks were initiated. For $P_{*1} \leqslant P < P_{*2}$, the search was conducted between l_t and b. For $P \geqslant P_{*2}$, the search was conducted for crack lengths greater than b.

6. Results

Figs 9 to 12 show the experimental l versus P behaviour for the four materials considered in Part I. The solid symbols represent indentation loads at which no cracks were observed (i.e. subthreshold indentations). The open symbols represent individual crack-length measurements. The upper and lower solid lines show the fitted upper and lower bounds, respectively. The central solid line is the mean response. Table II gives the corresponding values of the fitted parameters B, α_T, T_1, C_n and ψ_2. As an example, Fig. 13 is a plot of the residual and transformation stress distributions using the parameters from Table II and Equations

TABLE I Experimental fracture and deformation-parameters of Y–TZP materials

	Grain size, λ (μm)			
	0.27 ± 0.08	0.36 ± 0.13	0.42 ± 0.15	0.70 ± 0.30
Steady-state toughness, T_2 (MPa m$^{1/2}$)	4.2 ± 0.2	4.9 ± 0.1	5.4 ± 0.1	5.9 ± 0.3
Hardness, H (GPa)	12.3 ± 0.5	13.5 ± 0.3	13.4 ± 0.4	12.4 ± 0.3
Contact-impression tensile-zone size, S	0.266	0.267	0.267	0.294
Minimum trapped-crack length, l_t (μm)	9.6	3.4	2.6	1.4
Threshold indentation load, P_{*1} (N)	40	20	30	20
Escape indentation load, P_{*2} (N)	53	77	141	245
Well-developed crack parameter, P/l (N μm^{-1})	1.55	1.47	1.54	1.82

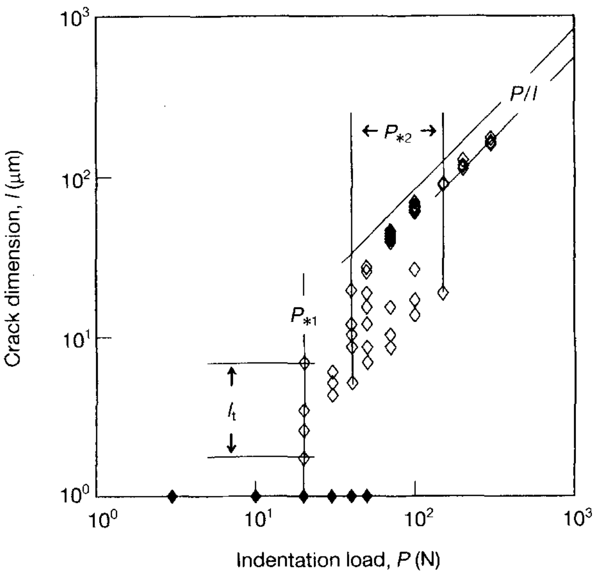

Figure 8 A plot of radial-crack length, l, versus indentation load, P, for a Y–TZP material (0.36 μm grain size). (◆) Subthreshold loads, and (◇) individual crack-length measurements. The solid lines indicate the bounds on the experimental variables used in fitting the model.

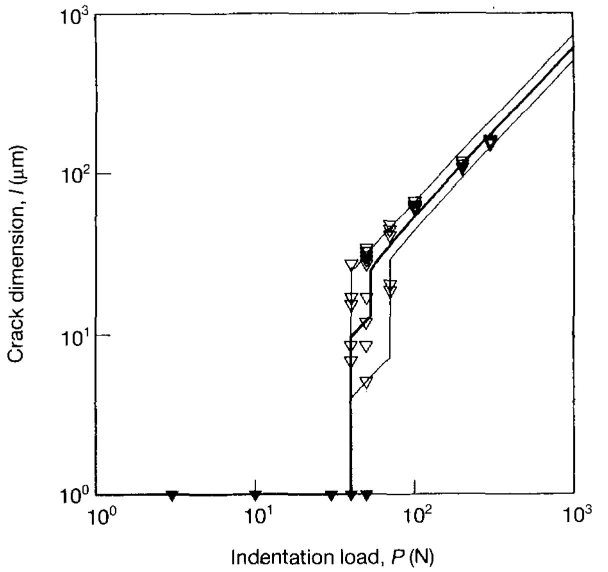

Figure 9 A plot of the radial-crack length, l, versus the indentation load, P, for a Y–TZP material (0.27 μm grain size). The upper and lower fine solid lines indicate the bounds of the predicted response from the indentation trapping model. The central bold solid line is the mean response. Key as defined in Fig. 1.

1–3. The inferred transformation stress for all the materials was of the order of 100 MPa, suggesting a volume fraction of monoclinic phase in the transformation zone of ~ 1%. This value compares with

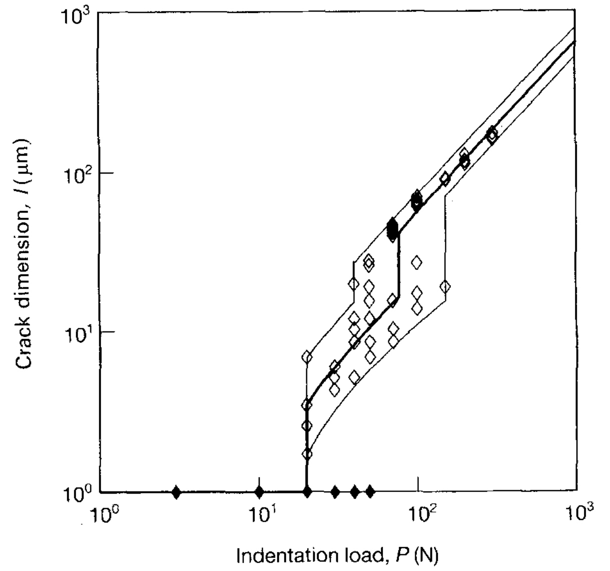

Figure 10 A plot of radial-crack length, l, versus indentation load, P, for a Y–TZP material (0.36 μm grain size). Key as defined as in Fig. 8.

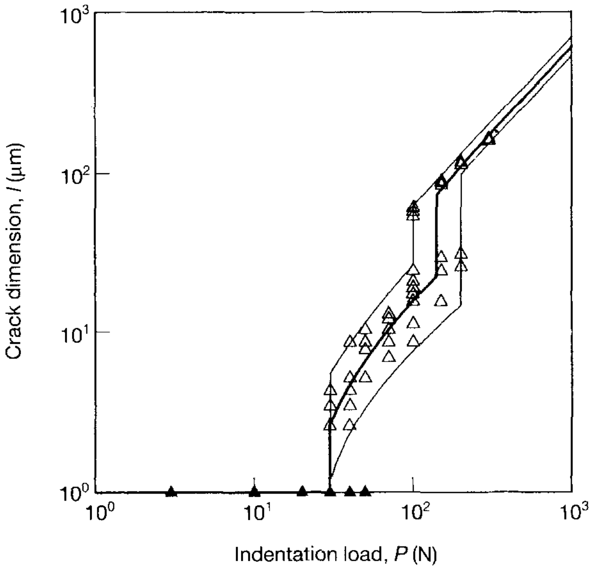

Figure 11 A plot of radial-crack length, l, versus indentation load, P, for a Y–TZP material (0.42 μm grain size). Key as defined in Fig. 1.

TABLE II Indentation crack initiation and trapping parameters of Y–TZP materials

	Grain size, λ (μm)			
	0.27 ± 0.08	0.36 ± 0.13	0.42 ± 0.15	0.70 ± 0.30
Transformation-zone dimension, B	0.428	0.526	0.727	0.775
Transformation stress coefficient, α_T	− 0.009	− 0.010	− 0.007	− 0.007
Transformation-zone toughness, T_1 (MPa $m^{1/2}$)	2.68	3.58	4.76	4.21
Contact-impression crack-nucleus dimension, C_n	0.211	0.241	0.259	0.294
Well-developed crack geometry factor, ψ_2	2.95	3.60	3.90	3.70

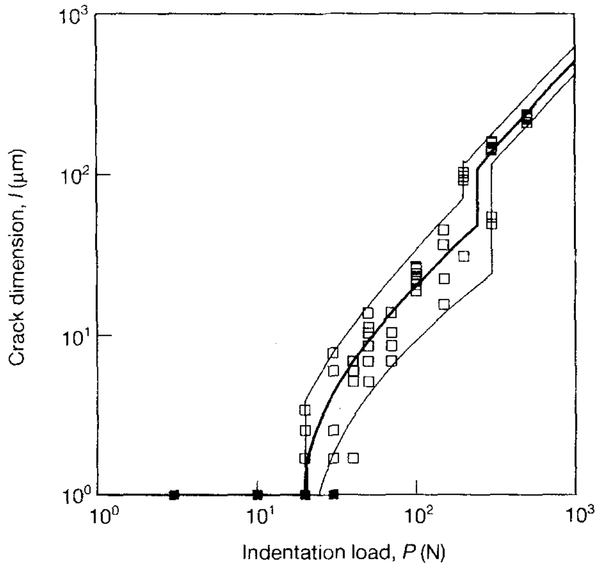

Figure 12 A plot of radial-crack length, l, versus indentation load, P, for a Y–TZP material (0.70 μm grain size). (■) Subthreshold loads, and (□) individual crack-length measurements.

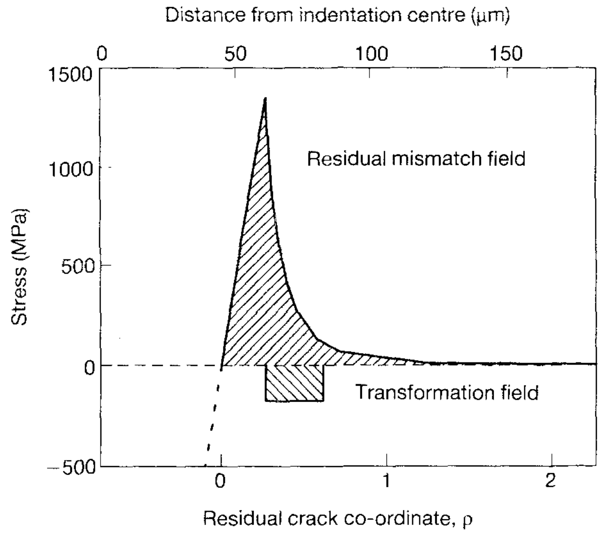

Figure 13 A plot of stress versus normalized radial-crack co-ordinate, ρ, for a Y–TZP material (0.36 μm grain size). The top axis gives the distance from the indentation centre for a 100 N indentation.

measurements by Raman spectroscopy of 2–5% in a 3Y-TZP [25].

Fig. 14 compares the mean $l(P)$ responses of the four materials. It is immediately apparent that the threshold indentation loads are similar but the indentation loads for cracks to escape to well-developed form increase with increasing grain size. This effect leads to a greater range of indentation loads in the large-grained materials over which cracks remain trapped.

In addition, there is a greater range of trapped-crack lengths about the mean response in the larger-grained materials. This latter effect is demonstrated in Fig. 15, which is a plot of the size of the transformation zone, B, and the minimum trapped-crack length, L_t, as a function of grain size. The symbols represent the mean responses and the error bars the upper and

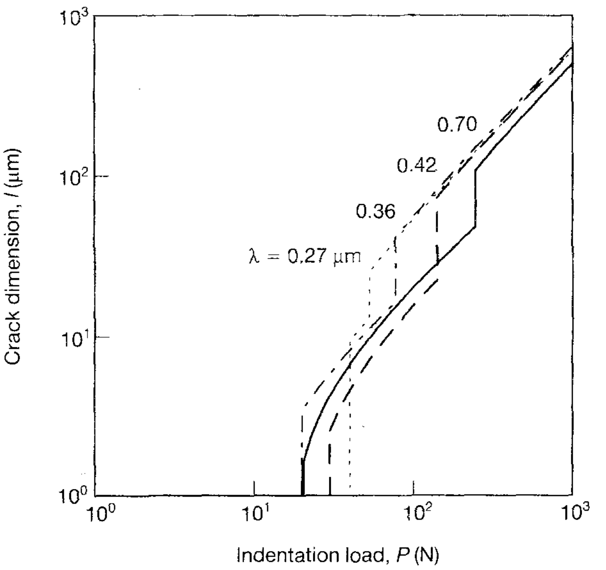

Figure 14 A composite plot of the mean radial-crack length response versus indentation load for Y–TZP materials with a range of grain sizes. As grain size increases, the indentation load for radial cracks to escape to well-developed form increases, thereby increasing the trapping-load range.

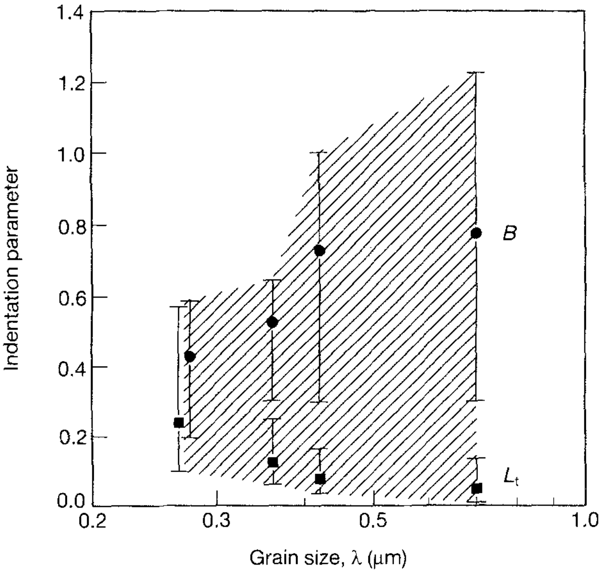

Figure 15 A plot of transformation zone size, B, and minimum trapped radial-crack length, L_t, as a function of grain size, λ, for Y–TZP materials. The divergence of these two parameters, emphasized by the hatched region, demonstrates the increasing range of trapped crack lengths with grain size.

lower bound values. The mean value of B increases with grain size, and the upper and lower bounds diverge. Conversely, the mean value of L_t decreases with grain size, and the bounds converge. The hatched region encompassing the lower bounds of L_t and the upper bounds of B represents the total range of trapped-crack lengths. This range diverges significantly with grain size, reflecting the increasing diversity with grain size in the length of the trapped cracks relative to the impression size, a.

Fig. 16 is an illustration of the diversity of the transformation-zone dimension and the trapped-crack lengths using these data. The hatched regions

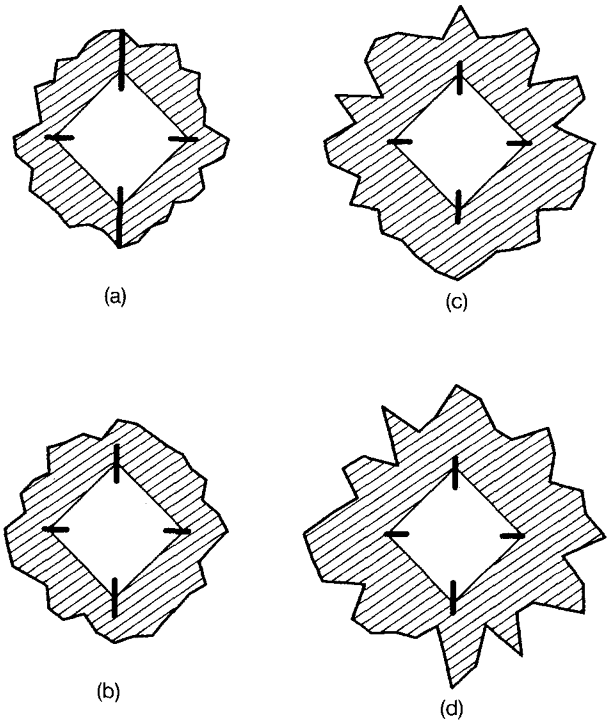

Figure 16 Schematic scale diagrams of indentations in Y–TZP materials showing the variability in the contact-induced transformation-zone radii (hatched regions) and the trapped-radial-crack lengths (solid lines). For grain sizes, λ, of: (a) 0.27 μm, (b) 0.36 μm, (c) 0.42 μm, and (d) 0.70 μm.

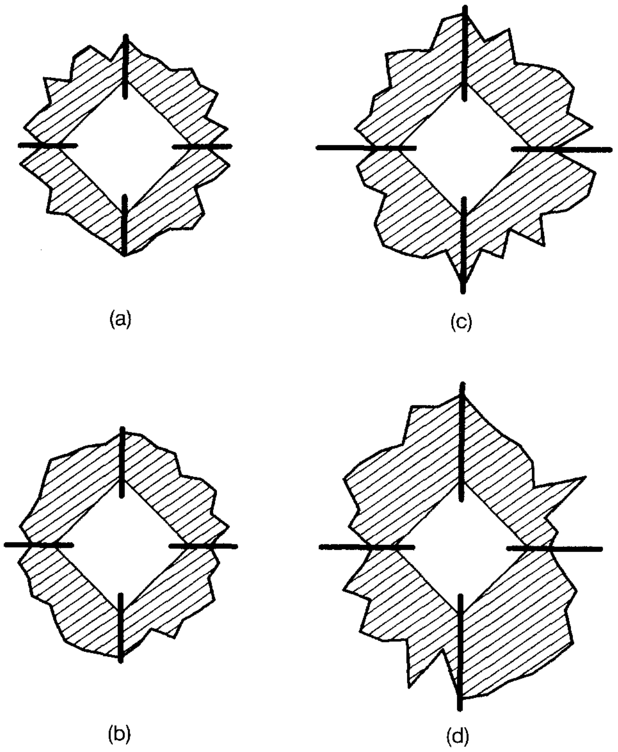

Figure 17 Schematic scale diagrams of indentations in Y–TZP materials showing the variability in the contact-induced transformation-zone radii (hatched regions) and the escaped radial-crack lengths (solid lines).

represent the contact-induced transformation zones (from random choices within the upper and lower bounds in 10° increments around the contact impression). The vertical solid lines represent the upper-bound lengths of the immediately post-threshold trapped cracks, and the horizontal lines represent the lower-bound lengths. Increases in the indentation load above the threshold configurations lead to trapped cracks between these lengths and the transformation-zone boundary. It is apparent that there is the possibility of greater indentation-to-indentation variability in the trapped-crack lengths with the larger-grain-size materials.

In comparison, there was very little indentation-to-indentation variability in the well-developed crack lengths. Fig. 17 is an illustration of the immediately post-escape, well-developed, crack configurations, with vertical and horizontal lines representing the upper and lower bounds as in Fig. 16. Increases in indentation load above these escape configurations lead to increases in the well-developed crack lengths (relative to the indentation dimensions) within the small limits set by these bounds. This reduced variability in the well-developed crack lengths extended to all the materials.

7. Discussion

The fracture-mechanics model developed here is clearly very capable of describing the variation of radial-crack lengths with indentation load in Y–TZP materials. While "goodness-of-fit" between the predictions and the experimental data (Figs 9–12) is no proof of the model, some of the parameters inferred from the model are in agreement with independent observations.

As noted, the magnitudes of the transformation stresses, σ_T, imply very small volume fractions of monoclinic phase in the contact-induced transformation zones in these materials. The low values of the transformed fractions hold the key to the ambiguity highlighted in Part I in attempts at indentation toughness measurements. Because the transformed fraction is small, the associated surface uplift is small (in most cases indiscernible), and hence it is not apparent that conventional indentation analyses will be inapplicable (especially as the cracks are usually very straight and visible). Thus, the distinction between trapped and well-developed cracks is not made, and both random (arising from the variability in the trapped crack lengths, e.g. see Fig. 16) and systematic (arising from an overestimate of the residual stress field acting on the well-developed cracks, e.g. see Fig. 13) errors are made. These errors have not extended to Ce–TZP and Mg–PSZ, as the transformed fraction is larger in these materials, leading to a greater surface uplift and obvious distortions of the residual field, and thus indentation toughness measurements are not even attempted.

The transformation-zone sizes inferred from the model also agree with other measurements. The extent of the surface uplift surrounding the contact impression in Fig. 2 in Part I provides a measure of the transformation zone and gives $0.64 < B < 1.24$ for the 0.70 μm grain-size material. This agrees with the bounds of $0.30 < B < 1.23$ inferred from the fit to the crack-length data.

To extend the comparison to other ZrO_2 materials, and to place the current materials in context, Fig. 18 is a plot of the transformation-zone size, B, against steady-state toughness T_∞ for this and other Y–TZP materials [1, 19, 25], Ce–TZP materials [25, 33, 34], and Mg–PSZ materials [35]. (B-values were determined from measurements of the surface uplift from published micrographs, and T_∞-values from reported large crack measurements.) The open symbols are the direct observation measurements, and the solid line is an empirical linear fit to these data. There is an obvious increase in the extent of contact-induced transformation with steady-state toughness. Extrapolation of the data to the zero-transformation zone, $B = 0$, yields a T_∞ value of ~ 2–$3\ \mathrm{MPa\,m}^{1/2}$ – very close to the lower-bound values observed for untoughened ZrO_2 [18] (and close to the lower bound for T_1 imposed here). As both the extent of the transformation zone and the toughening increment depend on the metastability or "transformability" of the tetragonal phase it is not surprising that they show the correlation in Fig. 18. The solid symbols are the zone sizes inferred from the fits, and they are obviously in agreement with the other measurements. (Extremely tough Mg–PSZ materials [36–38] do not follow the trend shown in Fig. 18, and they exhibit anomalously small transformation zones.)

Observations of fatigue in Mg–PSZ [39] show that crack motion is greatly affected by underloads or overloads in the cyclic loading. In particular, overloads cause significant decreases in crack velocity, suggesting that the cracks are "trapped" in a locally enhanced transformation zone and have difficulty "escaping" across the enhanced zone boundary, similar to the observations here. The implication is that subsequently stressed cracks in ZrO_2 materials, after generation by a sharp contact, will still retain the effects of the contact-induced transformation field, trapping the cracks.

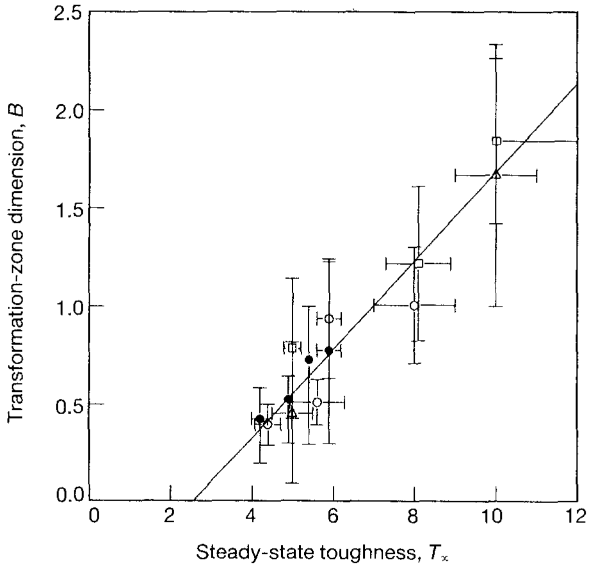

Figure 18 A plot of indentation transformation-zone size, B, versus steady-state toughness T_∞ for zirconia materials. The open symbols are direct experimental observations ((○) Y–TZP, (□) Ce–TZP, (△) Mg–PSZ) and (——) is a best fit to these data. (●) Results inferred from the indentation trapping model fits to crack-length measurements (Y–TZP).

If the strength-controlling flaws in a ZrO_2 component are cracks arising at sharp contacts, it is probable that cracks trapped in the compressive transformation zone will lead to greater strengths. A clear implication from the model is that in order to maximize trapping, α_T or B should be maximized. Fig. 18 suggests that an indication of the ability of a ZrO_2 material to trap cracks, and therefore exhibit less strength degradation by contact flaws, might be a large steady-state toughness. However, the greater variability of the degree of trapping (as indicated by the lengths of the trapped cracks) in materials with large transformation zones implies a trade-off in this regard – decreased strength degradation for a given contact size might be associated with increased strength variability at that contact. (That is, large toughnesses imply large transformation zones, which in turn imply greater strengths that have a lot of scatter.)

In closing, it should be noted that the model developed here is easily extended to other geometries (e.g. that of circular cracks), to modifications of the stress fields (e.g. extending the transformation field back into the contact impression), and to other systems. Examples of this latter include crack initiation in softer materials, such as ionic solids or semiconductors in which the compressive zone of a dislocation array may surround the contact impression, or spontaneous microcracking in inhomogeneous microstructures in which a compensating shield of compressive grains may surround the initiating tensile grain. Another obvious extension is the superposition of a uniform tensile field, in order to describe the behaviour of trapped cracks in components under stress [28].

Acknowledgements

The authors are grateful to W. C. Carter, B. R. Lawn, N. Padture, and M. D. Thouless for helpful discussions and suggestions during the course of this work and for reviews of the manuscript. Funding for LMB was partially supplied by the Center for Ceramics Research, Rutgers, The State University of New Jersey, Piscataway, NJ, USA.

References

1. R. F. COOK, L. M. BRAUN and W. R. CANNON, *J. Mater. Sci.* Part I, in press.
2. F. F. LANGE, in "Fracture mechanics of ceramics" Vol. 2, edited by R. C. Bradt, D. P. H. Hasselman and F. F. Lange (Plenum Press, New York, 1974) p. 599.
3. D. J. GREEN, in *ibid.* Vol. 5, edited by R. C. Bradt, A. G. Evans, D. P. H. Hasselman and F. F. Lange (Plenum Press, New York, 1983) p. 457.
4. M. V. SWAIN, *J. Mater. Sci.* **16** (1981) 151.
5. Y. FU, A. G. EVANS and W. M. KRIVEN, *J. Amer. Ceram. Soc.* **67** (1984) 626.
6. R. F. COOK and G. M. PHARR, in "Materials science and technology", Vol. 11, edited by M. V. Swain (VCH, Weinheim, 1994) p. 339.
7. D. R. CLARKE, *Acta Metall.* **28** (1980) 913.
8. B. R. LAWN and A. G. EVANS, *J. Mater. Sci.* **12** (1977) 2195.
9. J. T. HAGAN, *ibid.* **14** (1979) 2975.

10. S. S. CHIANG, D. B. MARSHALL and A. G. EVANS, *J. Appl. Phys.* **53** (1982) 298.
11. *Idem., ibid.* **53** (1982) 312.
12. K. TANAKA, *J. Mater. Sci.* **22** (1987) 1501.
13. W. CHENG and I. FINNIE, *ibid.* **25** (1990) 575.
14. S. LATHABAI, J. RÖDEL, T. DABBS and B. R. LAWN, *ibid.* **26** (1991) 2157.
15. F. C. FRANK and B. R. LAWN, *Proc. Roy. Soc. A* **299** (1967) 291.
16. R. MOUGINOT and D. MAUGIS, *J. Mater. Sci.* **20** (1985) 4354.
17. R. F. COOK and G. M. PHARR, *J. Amer. Ceram. Soc.* **73** (1990) 787.
18. D. J. GREEN, R. H. J. HANNINK and M. V. SWAIN, "Transformation toughening of ceramics" (CRC Press, Boca Raton, 1989).
19. T. R. LAI, C. L. HOGG and M. V. SWAIN, in "Ceramic developments", edited by C. C. Sorrell and B. Ben-Nissan, (Trans Tech Publications, Aedermannsdorf Switzerland, 1988) p. 1071; also in *Trans. Iron Steel Inst. Jpn.* **28** (1989) 240.
20. J. T. HAGAN and M. V. SWAIN, *J. Phys. D.* **11** (1978) 2091.
21. J. T. HAGAN, *J. Mater. Sci.* **15** (1980) 1417.
22. B. R. LAWN, T. P. DABBS and C. J. FAIRBANKS, *ibid.* **18** (1983) 2785.
23. H. M. CHAN and B. R. LAWN, *J. Amer. Ceram. Soc.* **71** (1988) 29.
24. M. Y. KHAN, L. M. BROWN and M. M. CHAUDHRI, *J. Phys. D* **25** (1992) A257.
25. M. J. REECE, P. L. TETLOW and C. GALIOTIS, *J. Mater. Sci. Lett.* **11** (1992) 575.
26. K. M. LIANG, G. ORANGE and G. FANTOZZI, *J. Mater. Sci.* **25** (1990) 207.
27. S.-Y. LIU and I.-W. CHEN, *J. Amer. Ceram. Soc.* **74** (1991) 1206.
28. L. M. BRAUN and R. F. COOK, in "Science and technology of zirconia V", edited by S. P. S. Badwal, M. J. Bannister and R. H. J. Hannink (Technomic, Lancaster, PA, USA, 1993) p. 386.
29. H. TADA, P. PARIS and G. R. IRWIN, "The stress analysis of cracks handbook", (Del Research, St. Louis, 1973).
30. M. T. LAUGIER, *J. Amer. Ceram. Soc.* **68** (1985) C-51.
31. R. F. COOK and E. G. LINIGER, *J. Mater. Sci.* **27** (1992) 4751.
32. R. M. ANDERSON and L. M. BRAUN, *J. Amer. Ceram. Soc.* **73** (1990) 3059.
33. K.-H. HEUSSNER and N. CLAUSSEN, *ibid.* **72** (1989) 1044.
34. D. B. MARSHALL, J. J. RATTO and F. F. LANGE, *ibid.* **74** (1991) 2979.
35. S. SRINIVASAN, R. O. SCATTERGOOD, G. PFEIFFER, R. G. SPARKS and M. A. PAESLER, *ibid.* **73** (1990) 1421
36. D. B. MARSHALL, M. R. JAMES and J. R. PORTER, *ibid.* **72** (1989) 218.
37. D. B. MARSHALL, *ibid.* **69** (1986) 173.
38. D. B. MARSHALL and M. R. JAMES, *ibid.* **69** (1986) 215.
39. R. H. DAUSKARDT, W. C. CARTER, D. K. VEIRS and R. O. RITCHIE, *Acta Metall. Mater.* **38** (1990) 2327.

Received 19 April
and accepted 16 August 1993